

Ca II Absorbers in the Sloan Digital Sky Survey: Statistics

Gendith M. Sardane^{1*}, David A. Turnshek¹, and Sandhya M. Rao¹

¹*Department of Physics and Astronomy and PITTsburgh Particle physics, Astrophysics, and Cosmology Center (PITT PACC), University of Pittsburgh, Pittsburgh, PA 15260*

ABSTRACT

We present the results of a survey for Ca II $\lambda\lambda 3934$, 3969 absorption-line systems culled from $\sim 95,000$ Sloan Digital Sky Survey (SDSS) Data Release 7 and Data Release 9 quasar spectra. With 435 doublets identified in the catalog, this list is the largest Ca II catalog compiled to date, spanning redshifts $z < 1.34$, which corresponds to the most recent ~ 8.9 Gyrs of the history of the Universe. We derive statistics on the Ca II rest equivalent width distribution and incidence (number density per unit redshift). We find that the $\lambda 3934$ rest equivalent width ($W_0^{\lambda 3934}$) distribution cannot be described by a single exponential function. A double exponential function is required to produce a satisfactory description. The function can be written as a sum of weak and strong components: $\partial n / \partial W_0^{\lambda 3934} = (N_{wk}^* / W_{wk}^*) \exp(-W_0^{\lambda 3934} / W_{wk}^*) + (N_{str}^* / W_{str}^*) \exp(-W_0^{\lambda 3934} / W_{str}^*)$. A maximum likelihood fit to the unbinned data indicates: $N_{wk}^* = 0.140 \pm 0.029$, $W_{wk}^* = 0.165 \pm 0.020$ Å, $N_{str}^* = 0.024 \pm 0.020$, and $W_{str}^* = 0.427 \pm 0.101$ Å. This suggests that the Ca II absorbers are composed of at least two distinct populations. The incidence (product of integrated absorber cross section and their co-moving number density) of the overall Ca II absorber population does not show evidence for evolution in the standard cosmology. The normalization of the no-evolution curve, i.e., the value of the Ca II incidence extrapolated to redshift $z = 0$, for $W_0^{\lambda 3934} \geq 0.3$ Å, is $n_0 = 0.017 \pm 0.001$. In comparison to Mg II surveys, we found that only 3% of Mg II systems in the SDSS have Ca II, confirming that it is rare to identify Ca II in quasar absorption-line surveys. We also report on some preliminary investigations of the nature of the two populations of Ca II absorbers, and show that they can likely be distinguished using their Mg II properties.

Key words: galaxies: individual: catalogs - quasars: absorption lines

1 INTRODUCTION

A successful and complete theory of galaxy formation and evolution must not only explain the properties of the luminous components of galaxies, but also account for the properties, kinematics, and evolution of gaseous structures associated with them. Quasar absorption lines (QALs) are an extremely powerful probe of the physical properties and kinematics of the gas in galactic, intergalactic and circumgalactic environments. Since the detection of gaseous structures in absorption is independent of the luminosity of the absorbing medium, quasar spectroscopy has been crucial in providing a wealth of information on the distribution and evolution of matter in the Universe. Without the selection bias caused by galaxy brightness and surface brightness limitations, one can identify structures that are fainter than what traditional imaging studies allow. QAL studies have resulted in the

identification of a gamut of intervening gaseous absorbers from the coolest molecular clouds detected in H₂ (e.g., Noterdaeme et al. 2008) to the predominantly neutral regions identified as H I damped Lyman alpha systems (DLAs) and low-ionization Mg II absorbers (e.g., Noterdaeme et al. 2012, Rao, Turnshek, & Nestor 2006, Quider et al. 2011, Seyffert et al. 2013), as well as hot ionized plasma in the extended halos of galaxies (e.g., Werk et al. 2014). The resonance transitions for the most common atoms and ions fall in the rest-frame ultraviolet (UV). Consequently, the QALs used to explore and make identifications of these various gaseous components studies have often concentrated on absorbers at moderate to high redshifts where these lines fall at wavelengths accessible to optical ground-based telescopes. Given available time allocations, the option of using space-based telescopes such as the Hubble Space Telescope (HST) to perform large UV QAL surveys is impractical, expensive, and unrealistic. Consequently, large statistical studies of absorp-

* E-mail: gms48@pitt.edu

tion line systems and the gaseous components of low-redshift galaxies that they trace are lacking.

One particular class of absorber, which falls at optical wavelengths at low redshift, is that traced by the Ca II H & K doublet, i.e. Ca II $\lambda\lambda 3934, 3969$. It is a resonance doublet transition of singly ionized calcium from the ground state with rest-frame wavelengths $\lambda = 3934.78$ Å (Ca II K) and $\lambda = 3969.60$ Å (Ca II H). The energy required to photoionize the neutral Ca atom is 6.11 eV. However, the energy required to photoionize Ca⁺ is only 11.87 eV, a value that is slightly less than the ionization potential of H I. Thus, Ca⁺ may not be the dominant ionization state of calcium. Moreover, Ca is a highly refractory element, being among the most depleted in the interstellar medium (Savage and Sembach 1996; Wild and Hewett 2005; Wild, Hewett & Pettini 2006). Thus, Ca II is a rare class of absorber, which nevertheless is an important diagnostic of key physical properties of the gas such as its density, degree of self-shielding, and dust content.

Strong Ca II absorption may preferentially arise in environments where some fraction of the dust grains has been destroyed, and the proportion of gaseous Ca has been enhanced by a large factor due to supernova-driven shocks associated with recent star-formation (Routly & Spitzer 1952). More recent studies of a handful of Ca II absorbers (Wild & Hewett 2005; Wild, et al. 2006; Wild, Hewett & Pettini 2007; Nestor et al. 2008; Zych et al. 2007; Zych et al. 2009) indicate that strong Ca II systems preferentially reside in dense, dusty, neutral, metal-rich, molecular H_2 -bearing environments - the reservoirs for subsequent star-formation. Moreover, measurements (Zhu & Menard 2013) of the average density profile of Ca II gas around galaxies out to ~ 200 kpc using cross-correlation analysis of the positions of $\sim 10^6$ foreground galaxies with $\sim 10^5$ background quasars in the Sloan Digital Sky Survey (SDSS) concluded that most of the Ca II in the Universe is in the circum- and intergalactic environments, and that the Ca II content in galaxy halos is larger for galaxies with higher stellar mass and star formation rates.

Studies of the extent of rare Ca II absorbers around galaxies will, therefore, place important empirical constraints on models for the existence of cool gas in the extended regions of galaxies. This includes models of cold accretion (e.g. Dekel & Birnboim 2006, Kereš et al. 2009, Stewart et al. 2011, and references therein) and models relying on radiation pressure driving from massive clusters followed by ram pressure driving from SNe (e.g. Nath & Silk 2009, Murray et al. 2011, Sharma & Nath 2012, and references therein), which can launch cool gas out beyond 50 kpc. These processes have implications for the fueling and evolution of galaxies (Davé, Oppenheimer & Finlator 2011; Davé, Finlator & Oppenheimer 2011, and references therein): cold accretion fuels star formation, while resulting feedback and outflows quench it. Furthermore, such studies are useful in understanding trends in the colors, luminosities, morphologies and orientations of galaxies, as well as the dust-content and metal-enrichment of the IGM/CGM. Since Ca II can be detected in ground-based surveys down to $z = 0$, the lowest redshift Ca II systems allow for detailed studies of the absorbers and their host galaxy environments.

In this paper, we present the results from the largest sample of Ca II $\lambda\lambda 3934, 3969$ absorbers ever compiled. In a blind survey of roughly 95,000 quasar spectra from the Seventh

and Ninth Data Release of the SDSS (SDSS-DR7, DR9), we identified 435 Ca II doublets with $W_0^{\lambda 3934} \geq 0.15$ Å. The wavelength coverage of the SDSS spectrum allows us to probe the redshift interval $z < 1.34$, which corresponds to ~ 8.9 Gyr of cosmic history. More importantly, Ca II gives us ground-based access to the low redshift regime of $z < 0.34$, equivalent to ~ 4 Gyrs of cosmic history, unlike any other commonly observed ionic transition.

The paper is organized as follows: In §2 we describe the data reduction process: the continuum fitting and line-finding algorithms, the selection criteria we imposed, and tests for systematic biases. We then present our main results in §3, where we derive the absorber rest equivalent width (REW) parametrization and evolution and the absorber redshift number density and its evolution, along with results on Ca II doublet ratios and how the incidence of Ca II absorbers compares with that of Mg II absorbers. In §4, we discuss evidence for two populations of Ca II absorbers. We summarize and present our conclusions in §5.

Throughout the paper, we assume a standard Λ CDM cosmology with $H_0 = 71$ km s⁻¹Mpc⁻¹, $\Omega_M = 0.27$, and $\Omega_\Lambda = 0.73$ (Spergel et al. 2007; Komatsu et al. 2011).

2 THE SDSS Ca II CATALOG

From its early beginnings, the SDSS (York et al. 2000) has been pivotal in advancing moderate resolution quasar absorption line spectroscopy by providing a huge increase in the number of quasar spectra available for absorption line surveys. Spectroscopy from the SDSS-I/II data releases has resulted in over 100,000 quasar spectra in the seventh data release (Schneider et al. 2010). The spectra were obtained using a pair of similar multi-object fiber spectrographs mounted on a dedicated 2.5-m wide-field telescope. Each spectrograph has 640 three-arcsecond-diameter fibers, with a combined spectral coverage of 3800 – 9200 Å. More recently, the ninth data release provided an additional $\sim 80,000$ quasar spectra (Ahn et al. 2012; Pâris et al. 2012) from ~ 1.5 years of data from the SDSS-III Baryon Oscillation Spectroscopic Survey (BOSS, Schlegel et al. 2007; Dawson et al. 2013). The improved BOSS spectrograph (Smee et al. 2013) has 1000 two-arcsecond-diameter fibers, and has an extended wavelength coverage of 3600 – 10,400 Å. Both the SDSS and BOSS spectrographs have approximately the same resolution ranging from 1500 at 3800 Å to 2500 at 9000 Å.

In this work, we utilize the most recent entries found in the SDSS DR7 and DR9 quasar catalogs of Schneider et al. (2010) and Pâris et al. (2012), respectively. The SDSS spectral coverage corresponds to an absorption redshift interval of $z < 1.34$ in the Ca II $\lambda 3934$ absorption line. We confined our search for Ca II absorption lines in the BOSS data set to redshifts $z < 1.34$ even though the BOSS quasar spectra have redshift coverage up to $z = 1.64$.

2.1 Quasar Sample Selection

In order to ensure adequate signal-to-noise ratios, we restricted the quasar sample to SDSS fiber magnitudes of $i < 20$, and to minimize the incidence of galaxies that have been misidentified as quasars, we only considered quasars

with $z_{em} \geq 0.1$. In addition, we searched for Ca II at wavelengths greater than 6000 km s^{-1} redward of the quasar Ly- α emission line. The quasar with the highest redshift in our sample has $z_{em} = 6.0$. We used the catalogs compiled by Shen et al. (2011) for SDSS DR7, and extended by Pâris et al. (2012) for SDSS DR9, to exclude broad absorption line quasars from our search. Altogether, 94,114 quasar spectra were useful for the search of the Ca II absorption doublet. The distribution of emission redshifts, z_{em} , of the quasar sample is shown in Figure 1. The distribution has a mean of $\langle z_{em} \rangle = 1.4$.

2.2 Data Reduction

The construction of our Ca II absorber sample closely follows the methods adopted for the construction of the University of Pittsburgh SDSS Mg II catalog described in Nestor et al. (2005), Rimoldini (2007), and Quider et al. (2011). Quite generally, our data reduction proceeds three-fold as follows: (1) automated quasar processing, (2) visual inspection of the automatically flagged doublet candidates, and (3) measurement of the line strengths of the doublets that passed the stringent visual inspection.

The automated processing procedure consisted of two stages, i.e., the pseudo-continuum normalization and the search for Ca II doublets. A combination of cubic splines and Gaussians were employed to determine the pseudo-continuum fit, which included both the true continuum as well as the broad emission features. In Figure 2, we show an example spectrum with the pseudo-continuum fit overplotted in red. For the vast majority of spectra, the continuum-fitter worked quite well, even in regions of poor signal-to-noise ratios. The error in the normalized flux is derived by dividing the flux error array by the fitted continuum. We do not propagate any errors in the continuum fit to determine the normalized error array. However, we will later show that a 20% error in continuum level determination is not the dominant source of uncertainty; given the relatively small number of detected systems, statistical Poisson errors are still the major source of uncertainty.

All normalized spectra are then searched for Ca II absorption using a line-finding algorithm that flags possible Ca II candidate doublets based on the doublet separation and line significance levels. To isolate a sample of intervening absorbers, we only accepted candidates that were separated in velocity by at least 6000 km s^{-1} from the quasar emission redshift, and from $z = 0$. Thus, biases that could arise due to an over-density of absorbers in the vicinity of quasar environments and the Milky Way, respectively, were minimized.

All candidate doublets were then visually inspected to check for satisfactory continuum fits, blends, and potential false detections due to the presence of absorption lines at other redshifts that could mimic the Ca II profile. We further note that we painstakingly examined each absorption feature flagged by the line-finding routine and retained systems after eliminating every other possibility. In order to identify a Ca II system, we required the detection of the $\lambda 3934$ line *and* the $\lambda 3969$ doublet partner. We required a 5σ minimum level of significance for the $\lambda 3934$ line and a 2.5σ minimum level of significance for the $\lambda 3969$ doublet partner. From their oscillator strengths, $f = 0.682$ for the $\lambda 3934$ line and $f = 0.330$ for the $\lambda 3969$ line (Kramida et al. 2013),

the secondary $\lambda 3969$ line is expected to be roughly half as weak as the primary $\lambda 3934$ line in the unsaturated regime. We measured the doublet REWs, $W_0^{\lambda 3934}$ and $W_0^{\lambda 3969}$, by fitting unresolved Gaussian profiles to both lines simultaneously, with full width half maxima (FWHM) given by the resolution of the SDSS spectrograph. Candidates with doublet ratios (DRs) that were outside the physically allowed range of $1.0 - \sigma_{DR} \leq W_0^{\lambda 3934}/W_0^{\lambda 3969} \leq 2.0 + \sigma_{DR}$ were eliminated. The error in the doublet ratio, σ_{DR} , was estimated assuming Gaussian uncertainties. The redshift of an absorber was determined from the weighted average of the wavelength centroids of the two fitted doublet Gaussian profiles. Figure 3 shows an example absorber that passed our selection cuts.

The survey sightline coverage, or sensitivity function, is shown in Figure 4 as a function of absorber redshift and minimum detectable REW threshold, W_0^{min} . The corresponding SDSS wavelength coverage is indicated by the top axis. The sightline coverage is the total number of lines of sight with sufficient signal-to-noise ratio to detect the $\lambda 3934 \text{ \AA}$ line with $W_0^{\lambda 3934} \geq W_0^{min}$ at a $\geq 5\sigma$ level of significance, *and, at the same time*, detect the $\lambda 3969 \text{ \AA}$ line at a $\geq 2.5\sigma$ level of significance. We emphasize that in order to be included in the accounting of the total survey path, a single redshift pixel and its corresponding doublet pixel position must have sufficient signal-to-noise ratios to detect the doublet pair at significance levels of 5σ and 2.5σ , respectively, and to detect both lines within the physically allowable doublet ratio range of $1.0 - \sigma_{DR} \leq W_0^{\lambda 3934}/W_0^{\lambda 3969} \leq 2.0 + \sigma_{DR}$.¹ The strongest possible $\lambda 3969$ absorption line is given by a profile with $DR = 1.0$, therefore, a pixel is rejected from the redshift path if a saturated $W_0^{\lambda 3969}$ line, where $W_{0,min}^{\lambda 3969} = W_{0,min}^{\lambda 3934}$, cannot be detected at this position with a significance level of at least 2.5σ . The sensitivity function for our survey is given by Equation 1:

$$g(W_0^{\lambda 3934}, z) = \sum_{i=1}^{N_{LOS}} H(z - z_{min(i)})H(z_{max(i)} - z) \times H[W_0^{\lambda 3934} - 5\sigma_0(z)]H[W_0^{\lambda 3969} - 2.5\sigma_0(z)] \quad (1)$$

where the sum is over the total number of lines of sight, N_{LOS} , and H is the Heaviside function. Using λ_{min} and λ_{max} to indicate the wavelength limit of each quasar spectrum, we write the minimum (maximum) redshift coverage, z_{min} (z_{max}), for each quasar spectrum as

$$z_{min} = \begin{cases} 0.02 & \text{if } \lambda_0 \geq \lambda_{min} \\ \lambda_{min}/\lambda_0 - 1 & \text{if } \lambda_0 < \lambda_{min} \end{cases} \quad (2)$$

$$z_{max} = \begin{cases} z_{em} - 0.02 & \text{if } \lambda_0(1 + z_{em}) < \lambda_{max} \\ \lambda_{max}/\lambda_0 - 1 & \text{if } \lambda_0(1 + z_{em}) \geq \lambda_{max}. \end{cases} \quad (3)$$

The prominent deep feature occurring near absorber redshift $z \sim 0.5$ (6000 \AA) is due to the dichroic (Schneider et al. 2010). The conspicuous absorption features redward of

¹ We note that no previous survey for absorption line doublets has imposed as stringent a doublet-finding criterion as employed here. Past surveys imposed a significance cut only on the stronger member of the doublet.

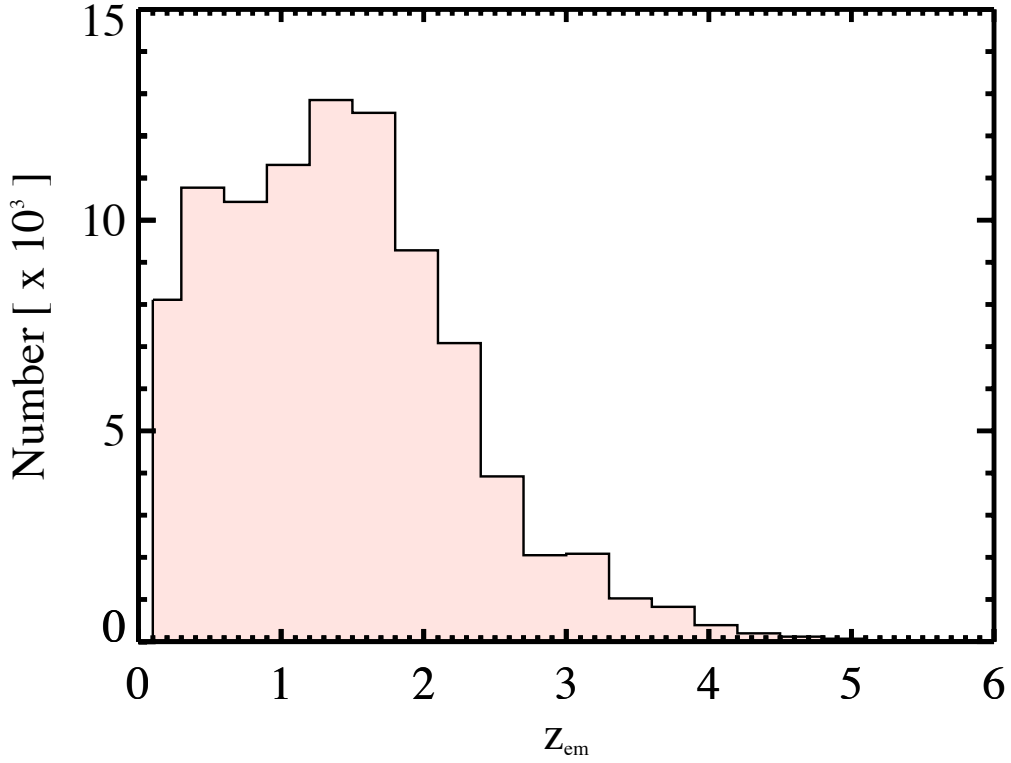


Figure 1. The distribution of emission redshifts of the SDSS quasars, with magnitudes $i < 20$ and $z_{em} \geq 0.1$, used to search for the Ca II $\lambda\lambda 3934, 3969$ absorption doublet. The distribution has a mean of $\langle z_{em} \rangle = 1.4$, and a maximum redshift of $z_{em} = 6.0$.

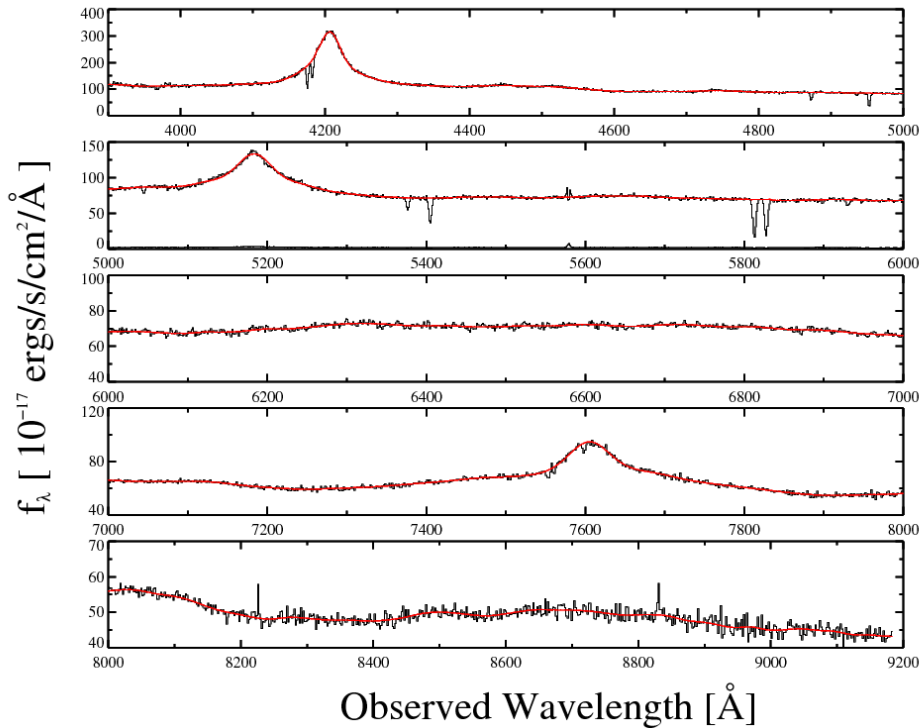


Figure 2. An example quasar spectrum with the pseudo-continuum fit overlaid in red. In this example, $z_{em} = 1.720$, and the median error is $\sim 2.6\%$ of the flux.

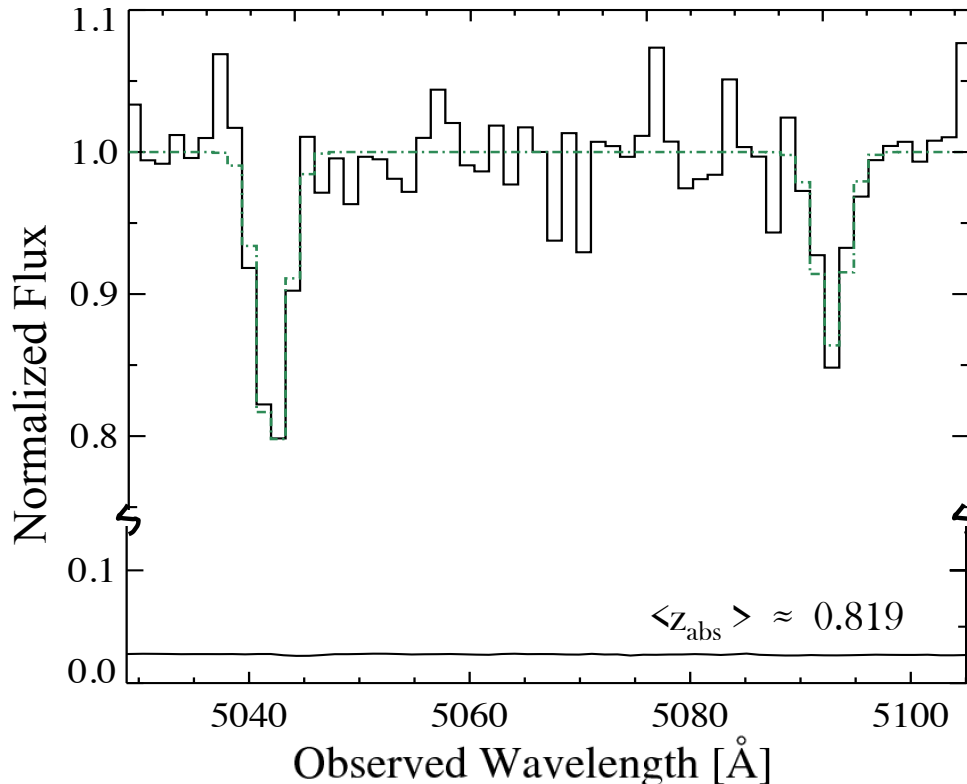


Figure 3. An example Ca II absorber system at $z_{abs} = 0.819$. The green dot-dash curve is a double Gaussian profile that was fit simultaneously to both members of the doublet. Note that to emphasize the feature, as well as its error array, the spectrum is truncated between $\sim 0.1 - 0.8$ in normalized flux units.

$z \sim 0.8$ are due to strong night sky lines in many spectra. Taking into account the line significance of both members of the Ca II doublet in calculating redshift path results in the doubling of narrow dips seen in Figure 4, as one might expect.

Integrating the sensitivity function of Figure 4 over the allowed redshift interval for Ca II, as determined by each SDSS spectrum, gives the cumulative path length of the survey, $g(W_0^{min})$, as a function of REW threshold W_0^{min} . The solid black curve shown in Figure 5 effectively describes the sensitivity of the survey to the measurement of a given strength of the $\lambda 3934$ line. For example, a $\lambda 3934$ line with REW $W_0^{\lambda 3934} \geq 1.0 \text{ \AA}$ can only be detected in roughly half of the total available sightlines. The sensitivity then asymptotes to 94,114 lines of sight at large REWs. The dash-dot black curve depicts the decrease in the cumulative path that would result from a (conservatively chosen) 20% error in the continuum fit, added to the flux error array in quadrature. The difference between the two paths peaks at 8% at $W_{min,0}^{\lambda 3934} = 0.2 \text{ \AA}$, decreases to 2% at $W_{min,0}^{\lambda 3934} = 1.0 \text{ \AA}$, and to 0.04% at $W_{min,0}^{\lambda 3934} = 6.0 \text{ \AA}$.

2.3 Monte Carlo Simulations to Determine False Positives and Systematics

We ran Monte Carlo simulations of the absorber catalog to test the efficiency of our detection routine and identify possible biases and systematic effects. Prior to the simulations, we masked out all detected Ca II systems from their

respective spectra, and used the edited spectra for the simulations instead. Using the observed distributions for the absorption redshift, $W_0^{\lambda 3934}$, and FWHM of the absorbers, and a uniformly distributed doublet ratio, we generated 10,000 Ca II doublets and inserted them into randomly-selected spectra. Approximately 7300 of these appeared in regions of spectra with sufficient signal-to-noise ratio that met our criteria for detection. We then ran the entire data pipeline and recovered 97.7% of these simulated doublets. Thus, we may have missed a maximum of 10 doublets in our search. In addition, no Ca II doublet that was not in the input list was falsely included in the output list of the simulation.

3 RESULTS

3.1 The $W_0^{\lambda 3934}$ Distribution

We identified 435 Ca II doublets with $W_0^{\lambda 3934} > 0.160 \text{ \AA}$ and $z \lesssim 1.34$. The first few entries of our Ca II catalog are presented in Table 1. The table is available in its entirety online. The observed $W_0^{\lambda 3934}$ distribution is shown in Figure 6. The strongest system we found has $W_0^{\lambda 3934} = 2.573 \text{ \AA}$, while the weakest system has $W_0^{\lambda 3934} = 0.163 \text{ \AA}$. The distribution has a mean of $\langle W_0^{\lambda 3934} \rangle = 0.769 \text{ \AA}$ and a spread of $\sigma = 0.393 \text{ \AA}$. Combining the observed distribution from Figure 6 with the sensitivity function in Figure 5, we obtain the sensitivity-corrected distribution for $W_0^{\lambda 3934}$, shown as the binned data points in Figure 7. The errors are determined using Poisson statistics. Similar to what has been found for

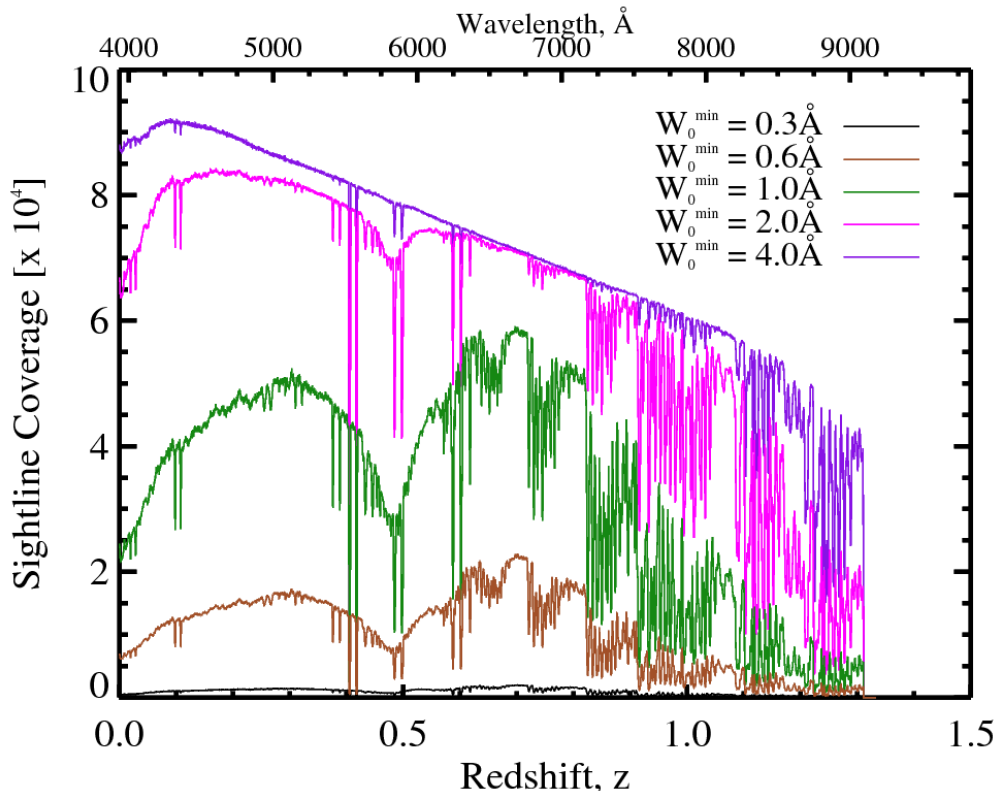


Figure 4. Sightline coverage for the Ca II survey in the SDSS DR9 as a function of absorber redshift and REW threshold: $W_0^{\min} = 0.3, 0.6, 1.0, 2.0, 4.0 \text{ \AA}$. This gives the total number of lines of sight with sufficient signal-to-noise ratio to detect at least a saturated Ca II doublet at the $5\sigma, 2.5\sigma$ significance levels. See text. The wide, deep feature near $z = 0.5$ is due to the SDSS dichroic. The sharp narrow dip in the middle of the dichroic is from the prominent O I $\lambda 5578$ night sky line. The series of sharp declines redward of $z \approx 0.8$ are due to strong night sky lines. The additional constraint on the $\lambda 3969$ line in Eq. 1 results in the doubling of narrow dips.

Table 1. The Ca II Sample^a

Quasar	SDSS g mag	z_{em}	z_{abs}	$W_0^{\lambda 3934}$ (\AA)	$\sigma(W_0^{\lambda 3934})$ (\AA)	$W_0^{\lambda 3969}$ (\AA)	$\sigma(W_0^{\lambda 3969})$ (\AA)
J001214.19–095922.9	19.44	1.262	0.6901	0.773	0.137	0.412	0.112
J001444.02–000018.5	17.95	1.550	0.0277	0.326	0.056	0.201	0.055
J002940.02+010528.5	17.83	1.388	0.3732	0.302	0.059	0.213	0.060
J004130.97+024222.5	18.81	2.308	0.7095	0.720	0.143	0.370	0.120
J004800.50+022514.9	18.96	2.160	0.5982	0.594	0.101	0.297	0.096

^aThe table is available in its entirety online.

other classes of QAL systems, the REW distribution rises with decreasing REWs. However, the data clearly show a change in the slope of the distribution near $W_0^{\lambda 3934} \approx 0.9 \text{ \AA}$. The best-fit single exponential function, determined using a maximum likelihood estimate (MLE) on the unbinned data, is clearly a poor fit as shown by the red dotted line in Figure 7. Therefore, we used a double-exponential function, written as the sum of weak and strong components, to obtain a satisfactory fit. Equation 4 parametrizes the model with two characteristic REWs, a W_{wk}^* and W_{str}^* , and two normalization constants, N_{wk}^* and N_{str}^* , for the weak and strong components, respectively.

$$\frac{\partial n}{\partial W_0^{\lambda 3934}} = \frac{N_{wk}^*}{W_{wk}^*} e^{-\frac{W_0^{\lambda 3934}}{W_{wk}^*}} + \frac{N_{str}^*}{W_{str}^*} e^{-\frac{W_0^{\lambda 3934}}{W_{str}^*}} \quad (4)$$

The resulting fit parameters are $N_{wk}^* = 0.140 \pm 0.029$ and $W_{wk}^* = 0.165 \pm 0.020 \text{ \AA}$ for the weak component, and $N_{str}^* = 0.024 \pm 0.020$ and $W_{str}^* = 0.427 \pm 0.101 \text{ \AA}$ for the strong component. The solid green curve shows this best-fit double exponential function MLE fit to the unbinned data. The dashed grey lines are the two individual components; from this fit, we determined that the change in slope occurs at $W_0^{\lambda 3934} = 0.88 \text{ \AA}$.

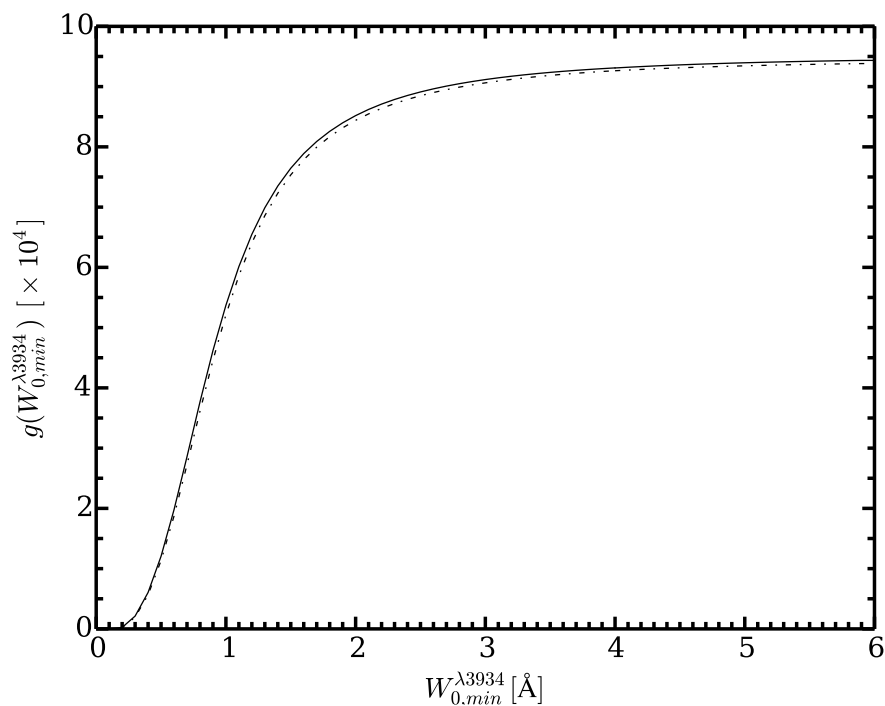


Figure 5. The cumulative path length, $g(W)$, as a function of REW threshold is shown here as the black solid curve. The decrease in the path due to an additional 20% uncertainty in the pseudo-continuum fit added in quadrature is shown by the black dash-dot curve. The difference between the two cumulative path lengths peaks at 8% at $W_{0,min}^{\lambda 3934} = 0.2 \text{ \AA}$, decreases to 2% at $W_{0,min}^{\lambda 3934} = 1.0 \text{ \AA}$, and to 0.04% at $W_{0,min}^{\lambda 3934} = 6.0 \text{ \AA}$.

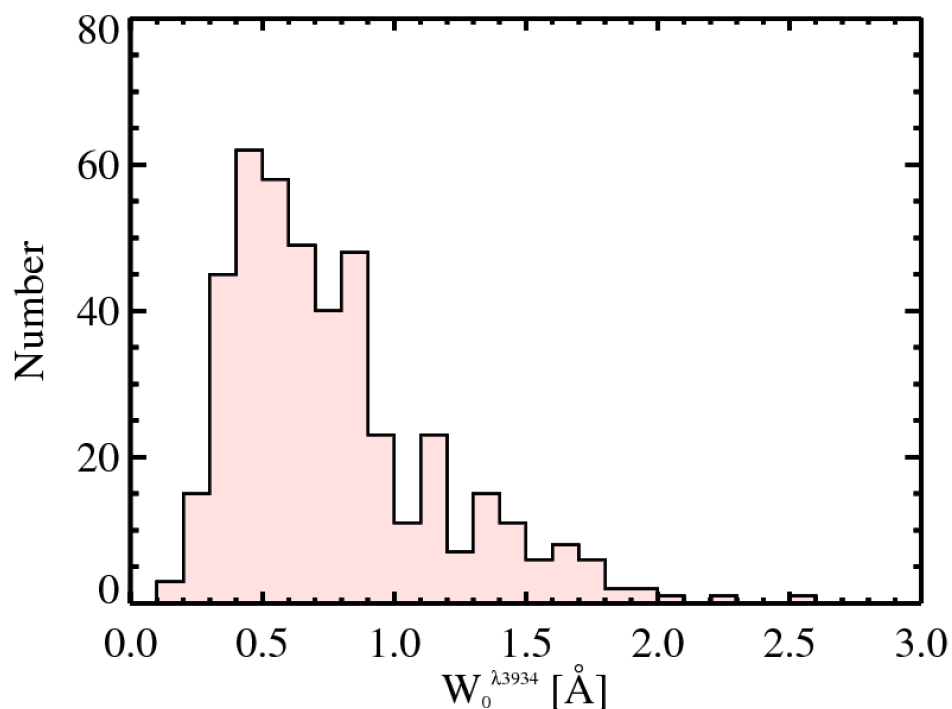


Figure 6. The observed REW distribution for $W_0^{\lambda 3934}$. The distribution has a mean of 0.769 \AA and a spread of 0.393 \AA . Measured REWs range from $0.163 \text{ \AA} \leq W_0^{\lambda 3934} \leq 2.573 \text{ \AA}$.

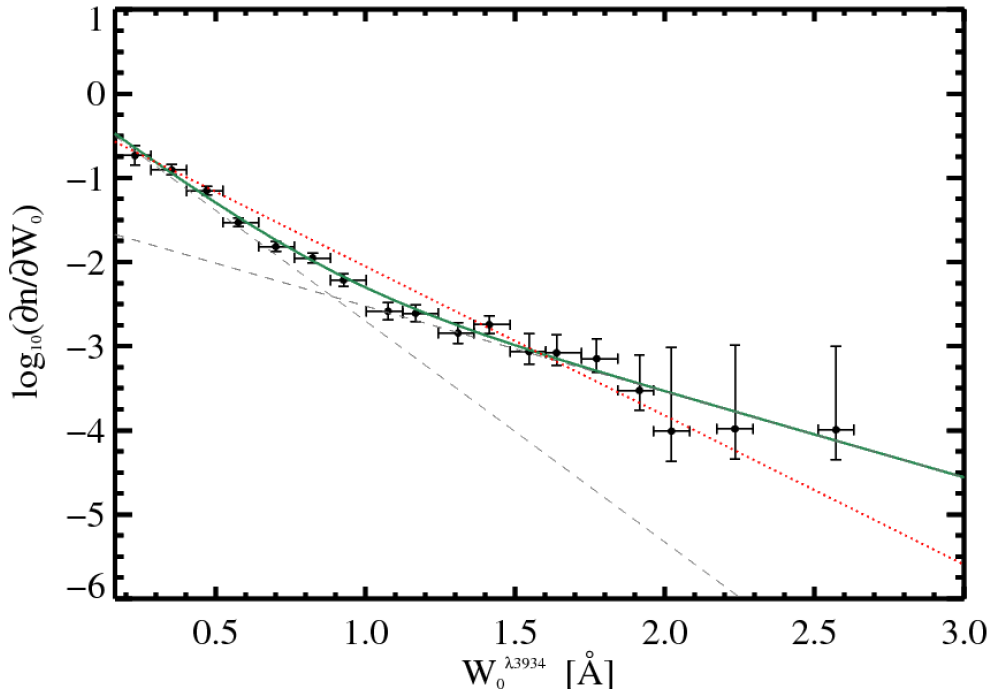


Figure 7. The sensitivity-corrected $W_0^{\lambda_{3934}}$ distribution. The double exponential model, Equation 4, that maximizes the likelihood to the unbinned data, is shown in green. The two single-exponential components of Equation 4 are plotted as grey dashed lines. The maximum likelihood fit using a single exponential model is shown as the red dotted line.

We evaluated the Akaike Information Criterion (AIC) for both the single and double exponential fits, and obtained $AIC = 46$ and $AIC = 11$ for the two fits, respectively. The AIC is a measure of the quality of the candidate models relative to each other (Liddle 2007). It is based on information entropy and quantifies the trade-off between goodness of fit and complexity (i.e., the number of parameters) of the model. Given a set of candidate models, the model with the smallest AIC value has the strongest support. Thus based on the AIC values above, the data are significantly better represented by the double exponential fit. The existence of a change in slope and the success of the double exponential model may be interpreted as evidence for the existence of more than one class of Ca II absorber. We will address this possibility further in §4.

3.1.1 Redshift Evolution of $\partial n/\partial W_0$

We now investigate the redshift evolution of the REW distribution, $\partial n/\partial W_0$. We binned the data into three redshift subsamples, with each z_{abs} interval having roughly the same number of absorbers. The results are shown in Figure 8. The solid green curves show the MLE fit to the unbinned data. For comparison, the single exponential fits are shown as red dashed lines. The subsample in the lowest redshift bin shows the most prominent departure from a single exponential fit. While the other two subsamples still show some hints of a change in slope, it is less apparent given the increasing size of the error bars at larger $W_0^{\lambda_{3934}}$. The AIC values in each subsample suggest that the single exponential model is still less favored, although the degree of support has decreased in the higher-redshift subsamples. Thus, we cannot

discount the possibility of the persistence of multiple populations across the different redshifts.

In Figure 9 we plot the resulting double exponential model parameters W_{wk}^* and W_{str}^* , and N_{wk}^* and N_{str}^* , as a function of the mean z_{abs} in each subsample. The result for the entire Ca II sample is shown as the open data points, plotted at a z_{abs} that is slightly offset from the median for clarity. These plots clearly show that there is no evidence for evolution in the shape of the exponential distributions for either the weak or strong components of the fit. In addition, Kolmogorov-Smirnov (KS) tests are also consistent with no evolution.

3.2 The Ca II Absorber Redshift Distribution

The observed absorber redshift distribution is shown in Figure 10. As mentioned previously, SDSS spectra can be used to search for Ca II at redshifts $z_{abs} \lesssim 1.34$, equivalent to a lookback time of $t_{LB} = 8.9$ Gyrs, or $\gtrsim 60\%$ of our cosmic history. The observed distribution has a mean redshift of $\langle z_{abs} \rangle = 0.579$, and standard deviation of $\sigma_{z_{abs}} = 0.296$. The distinct drop in sensitivity near $z \sim 0.5$ is mainly due to the SDSS dichroic.

The number density, $\partial n/\partial z$, or the incidence of lines that have $W_0^{\lambda_{3934}}$ larger than a specified threshold W_0^{min} over some redshift interval, is given by

$$\left. \frac{\partial n}{\partial z} \right|_{W_0 > W_0^{min}} = \sum_{\substack{W_{0,i} > W_{0,min} \\ z_i \in (z, z+dz)}} \frac{1}{g(W_{0,i}, z_i) dz} \quad (5)$$

whose variance is given by

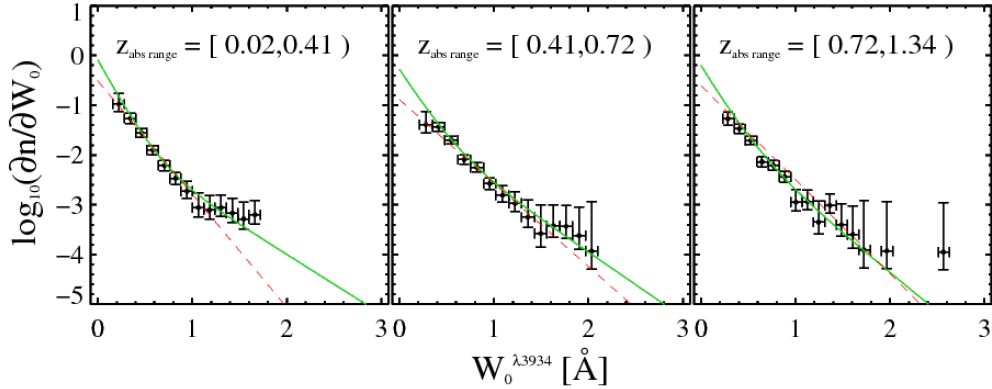


Figure 8. The sensitivity-corrected $W_0^{\lambda_{3934}}$ distribution binned into three redshift intervals. The double exponential model (Equation 4) that maximizes the likelihood to the unbinned data is shown in green. The single exponential model is shown as the red dashed line. The single exponential model is less favored over the double exponential model in all redshift intervals.

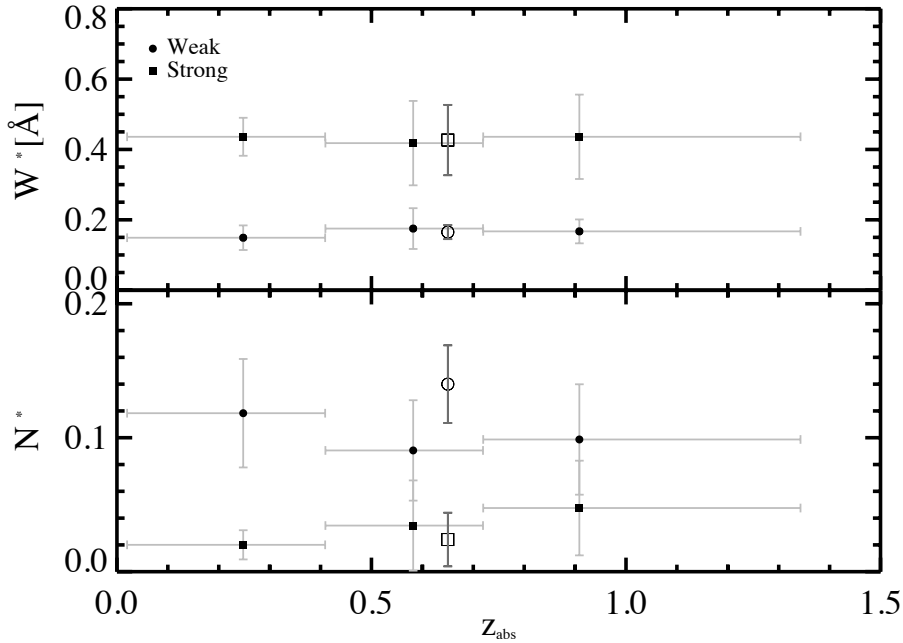


Figure 9. *Top:* The MLE characteristic REWs, W^* , for the weak (filled circles) and strong (filled squares) components, in the three redshift ranges shown in Figure 8. The error bars and bin sizes are shown in grey. The W^* parameters imply a lack of redshift evolution in the slopes of each component. *Bottom:* The MLE normalizations for the two-component fit, which within the errors, are also consistent with no evolution. For reference, we have plotted the results for the entire sample as open circles and squares, which for clarity, are plotted at a location slightly offset from the median z_{abs} .

$$\sigma^2 = \sum_{\substack{W_{0,i} > W_{min}^0 \\ z_i \in (z, z+dz)}} \left(\frac{1}{g(W_{0,i}, z_i) dz} \right)^2. \quad (6)$$

We reiterate that one can ignore the errors in $g(W, z)$ since the dominant contribution to the error budget comes from the number counts, as discussed in §2.2. The incidence of absorption lines represents the product of the in-

tegrated number density of absorbers per co-moving volume and their effective cross section. Figure 11 shows the Ca II incidence for various equivalent width thresholds, $W_0^{\min} = 0.3, 0.6, 1.0, 1.5 \text{ \AA}$. In each panel, the data are binned to have approximately equal numbers of systems. In each panel, the dash-dot lines show the no evolution curves (NECs) predicted by the standard cosmology (Equation 7). The normalization, n_0 , has been adjusted to minimize the sum of squared deviations of the binned data

points from the curve. For $W_0^{\lambda 3934} \geq 0.3 \text{ \AA}$, the normalization constant, which is also the extrapolated incidence at $z = 0$, is $n_0 = 0.017 \pm 0.001$. Except for the case where $W_0^{\lambda 3934} \geq 1.5 \text{ \AA}$, the data are consistent with the NEC at better than the 99.9% confidence level.

$$\frac{dn}{dz} = n_0 \frac{(1+z)^2}{\sqrt{\Omega_M(1+z)^3 + \Omega_\Lambda}} \quad (7)$$

3.3 The Ca II Doublet Ratio

For transitions with different oscillator strengths (e.g., absorption doublets), a measured doublet ratio (DR) is an important indicator of the degree of saturation of an absorption line. The equivalent widths of weak unsaturated lines provide direct measurements of column densities. For strong, saturated doublets, such as Mg II $\lambda\lambda 2796, 2803$ and Fe II $\lambda\lambda 2586, 2600$, equivalent width measurements are more appropriately related to gas velocity spreads. The observed Ca II DRs ($W_0^{\lambda 3934}/W_0^{\lambda 3969}$) for our sample range from ~ 2 for completely unsaturated systems to ~ 1 for completely saturated systems. The left panel in Figure 12 shows the DR distribution for our sample. It has a mean of ~ 1.7 and a spread of $\sigma_{DR} \sim 0.4$. Hence, the Ca II doublets are on average between the two extreme possible values. The right panel in Figure 12 shows $W_0^{\lambda 3969}$ versus $W_0^{\lambda 3934}$ and includes the errors on these observed values, with the dash-dot lines bounding the physically allowed DR ranges, as in the left panel. Figure 13 shows the DRs as a function of redshift, along with the propagated DR errors assuming Gaussian error distributions. There is no detectable evolution in the DR distribution.

3.4 The Ca II versus Mg II Incidence

To make appropriate comparisons of the Mg II incidence to that of Ca II, we first determine which of the Ca II systems in our sample have confirmed Mg II measurements. We made use of the data available from the University of Pittsburgh SDSS DR4 Mg II Catalog (Quider et al. 2011), extended up to SDSS DR7 (E. Monier, private communication). In total, the extended Mg II catalog contains over 29,000 doublets, which includes an additional $\sim 13,000$ unique Mg II systems from SDSS DR7. The Quider et al. (2011) Mg II sample was selected based on 5σ and 3σ significance cuts for $W_0^{\lambda 2796}$ and $W_0^{\lambda 2803}$, respectively. A similar doublet ratio cut of $1.0 - \sigma_{DR} \leq W_0^{\lambda 2796}/W_0^{\lambda 2803} \leq 2.0 + \sigma_{DR}$ was also imposed to construct the final catalog. For absorbers from SDSS DR9, we measured the strengths of the Mg II doublets, and made the appropriate cuts. Note that to find Mg II, the Ca II system must be at $z_{abs} \gtrsim 0.4$. However, detecting the corresponding Mg II lines also depends on the quasar emission redshift and the SNR of the spectrum at the predicted Mg II location. Lines that fell in the Ly α forest were not measured. After implementing the required selection cuts, we have 251 Ca II-Mg II systems. The results are shown in Figure 14. We see a positive correlation between the strengths of the two lines, albeit with a spread that is quite large. However, the distribution does appear to have a sharp lower bound. The three dash-dot lines have $W_0^{\lambda 2796}/W_0^{\lambda 3934} = [1, 2, 4]$.

We also performed the reverse search where we looked for Ca II lines corresponding to Mg II systems from DR7 in the $0.4 \leq z \leq 1.34$ redshift interval. Only 3% of Mg II systems were found to have Ca II, confirming that it is rare to identify Ca II in quasar absorption-line surveys.

We now compare the incidence of Ca II absorbers to the more common Mg II systems. In Figure 15, the incidence of Ca II is shown as the green data points using the following REW thresholds: $W_0^{\lambda 3934} \geq 0.3 \text{ \AA}$ shown on the top panels, and $W_0^{\lambda 3934} \geq 0.6 \text{ \AA}$ shown by the bottom panels. The Mg II incidence is shown in red. The errors are derived using Poisson counting statistics. Within each panel, we binned the data so that each point has roughly the same number of systems. Note that these are plotted against t_{LB} in the linear scale instead of z_{abs} in order to highlight the length of cosmic time that Mg II cannot trace using ground-based optical observations. Motivated by the observed ratios in Figure 14, we have chosen the following Mg II-Ca II ratios: $W_0^{\lambda 2796}/W_0^{\lambda 3934} = [2, 4]$ for this comparison. For both absorbers, the NECs were normalized to minimize the sum of the squares of the residuals. The resulting fits are consistent with the data at $\gtrsim 99\%$ confidence level for both absorbers at all REW thresholds. The Ca II incidence is in a sense similar to Mg II in that the gaseous cross-sections do not show evidence for evolution at $z_{abs} > 0.4$, and with this new result from Ca II, we extend the same conclusions down to $z = 0$. Figure 15 also underscores the rareness of Ca II absorbers relative to Mg II. More specifically, in the left panels of Figure 15, where $W_0^{\lambda 2796} = 2W_0^{\lambda 3934}$, the incidence of Ca II is roughly a factor of ~ 10 times smaller. At the larger REW ratios (right panels), as the number of stronger Mg II absorber becomes rare, this fraction drops to a factor of ~ 3 to 4.

4 INVESTIGATING THE POSSIBILITY OF TWO Ca II ABSORBER POPULATIONS

The $W_0^{\lambda 3934}$ distribution shown in Figure 7 reveals a break in $\partial n/\partial W_0^{\lambda 3934}$ at $W_0^{\lambda 3934} = 0.88 \text{ \AA}$. The need for a strong and a weak component to adequately fit the overall distribution (Equation 4) suggests that we should investigate trends which might further reveal the properties of these components. Below we search for identifiable trends based on: (1) the $W_0^{\lambda 3934}$ value and Ca II DR, and (2) the $W_0^{\lambda 3934}$ value and the Mg II-to-Ca II ratio ($W_0^{\lambda 2796}/W_0^{\lambda 3934}$).

4.1 Trends with $W_0^{\lambda 3934}$ and Ca II DR

Here we explore the possible role of the Ca II DR in isolating the two components of the $W_0^{\lambda 3934}$ distribution. To do this we divide the entire Ca II sample into four subsamples of roughly equal size based on their DRs and $W_0^{\lambda 3934}$ values. This can be accomplished by making divisions above and below $DR = 1.5$ and $W_0^{\lambda 3934} = 0.7 \text{ \AA}$. Note that these values lie close to the mean doublet ratio of the entire sample and the location of the break in Figure 7.

In Figure 16, we plot the sensitivity-corrected $W_0^{\lambda 3934}$ distributions for the four defined subsamples. The resulting four distributions can now be accurately parametrized by single exponential functions. The best-fit single exponential functions to the unbinned data are shown as dash-dot lines.

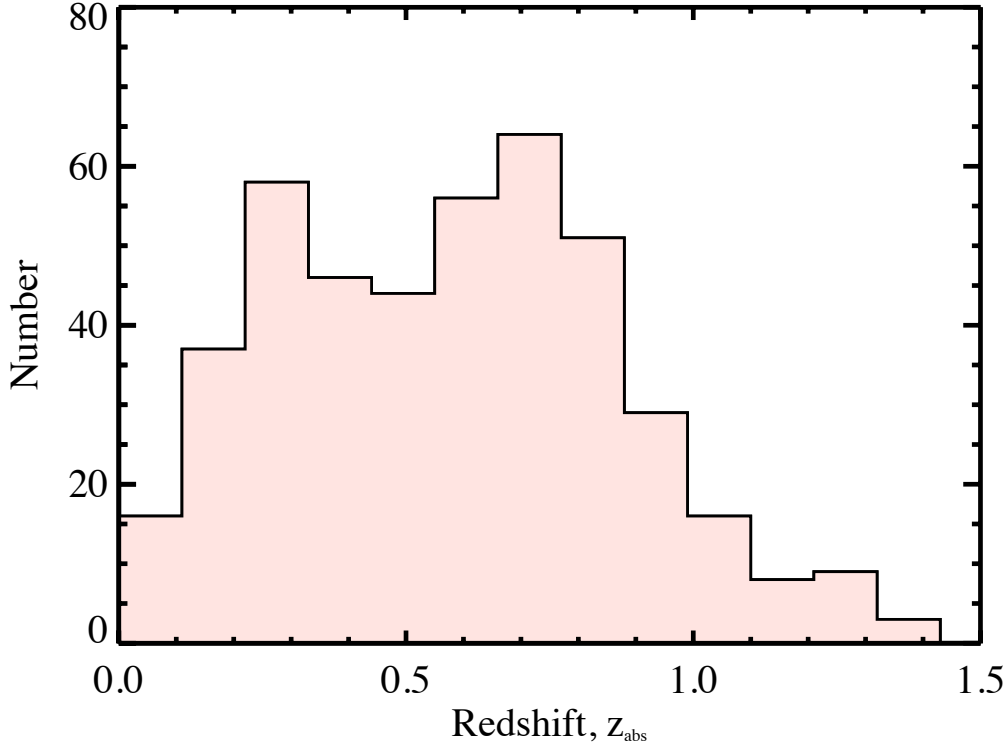


Figure 10. The observed absorber redshift distribution shown in bins of $\Delta z = 0.1$, with mean $z_{abs} = 0.579$ and standard deviation $\sigma = 0.296$. The poor SNR of SDSS spectra near $z_{abs} \sim 0.5$, due to the SDSS dichroic, causes the decrease in the number of detected Ca II systems that pass our selection criteria at this redshift.

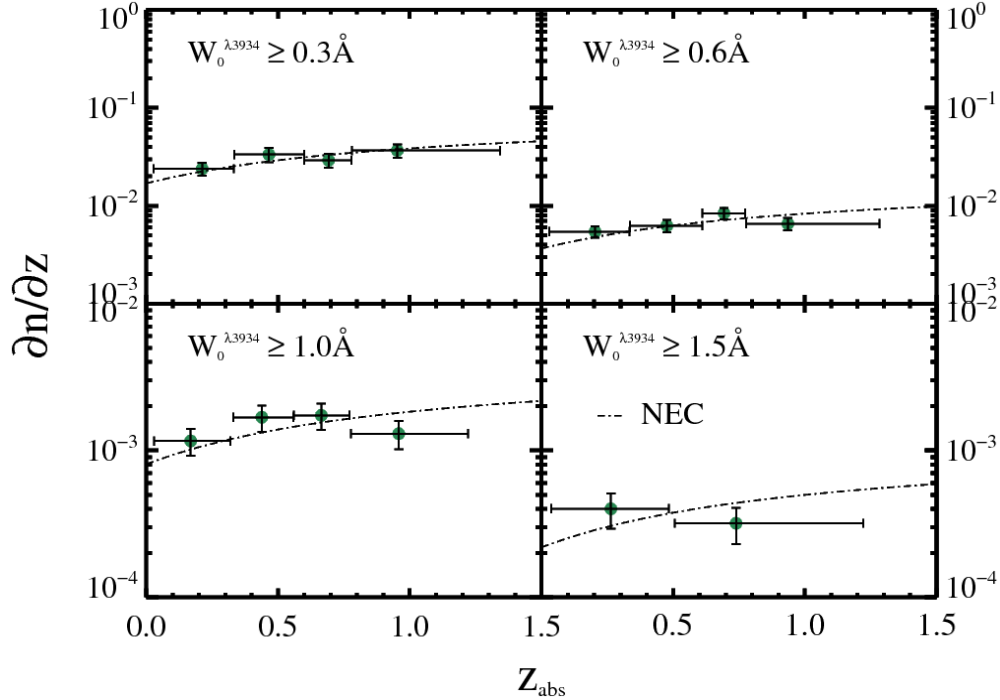


Figure 11. The Ca II redshift number density as a function of z_{abs} for various REW thresholds $W_0^{\lambda_{3934}} \geq W_0^{min}$. The errors are determined using Poisson statistics. The bin sizes are such that there are approximately equal numbers of systems in each bin. The no evolution curves (NEC) are shown as dash-dot lines. The NECs are normalized to minimize the sum of squared deviations of the binned data from the curve. With the exception of the $W_0^{\lambda_{3934}} \geq 1.5 \text{ \AA}$ sample, the NECs are consistent with the data at a $> 99.9\%$ significance level. The $W_0^{\lambda_{3934}} \geq 1.5 \text{ \AA}$ sample has too few data points to allow for a meaningful interpretation.

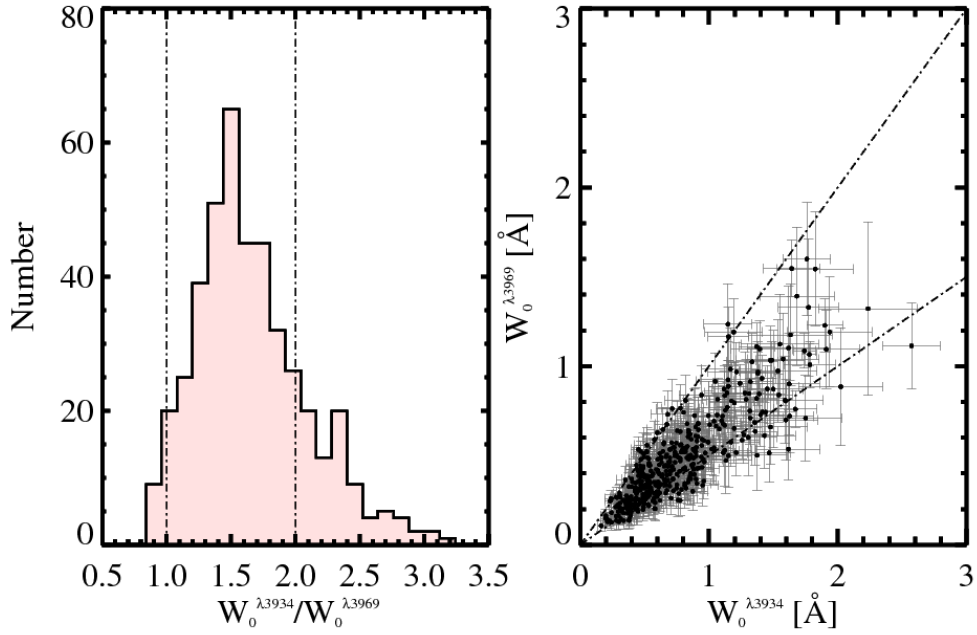


Figure 12. *Left:* The $W_0^{\lambda 3934}/W_0^{\lambda 3969}$ doublet ratios for the Ca II sample. The dash-dot lines mark the limits of 1.0 for completely saturated systems and 2.0 for completely unsaturated systems. Values above and below these limits are due to poorer signal-to-noise ratio data. Our sample is not dominated by either extreme DR values. *Right:* $W_0^{\lambda 3934}$ vs. $W_0^{\lambda 3969}$.

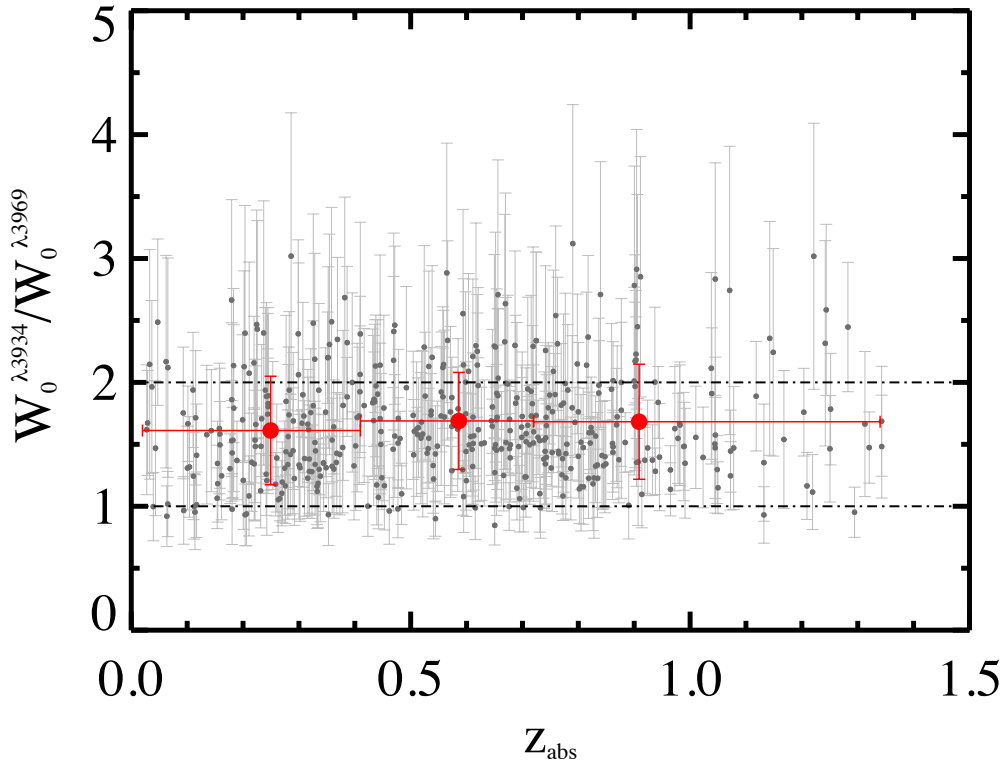


Figure 13. The $W_0^{\lambda 3934}/W_0^{\lambda 3969}$ doublet ratio as a function of redshift for Ca II systems. There is no detected redshift evolution in the doublet ratio.

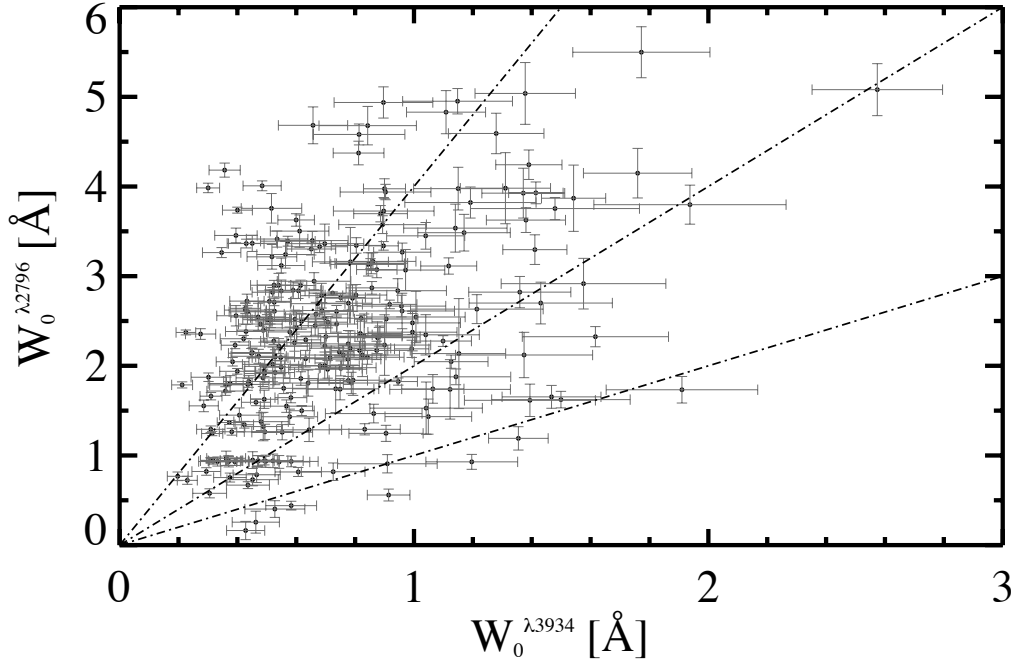


Figure 14. $W_0^{\lambda 2796}$ versus $W_0^{\lambda 3934}$ for the 251 Ca II systems in our sample with detected Mg II. See text. There is a correlation between the REWs of Mg II with Ca II, albeit with a large spread, but a sharp lower bound. The three dash-dot lines have $W_0^{\lambda 2796}/W_0^{\lambda 3934} = [1.0, 2.0, 4.0]$.

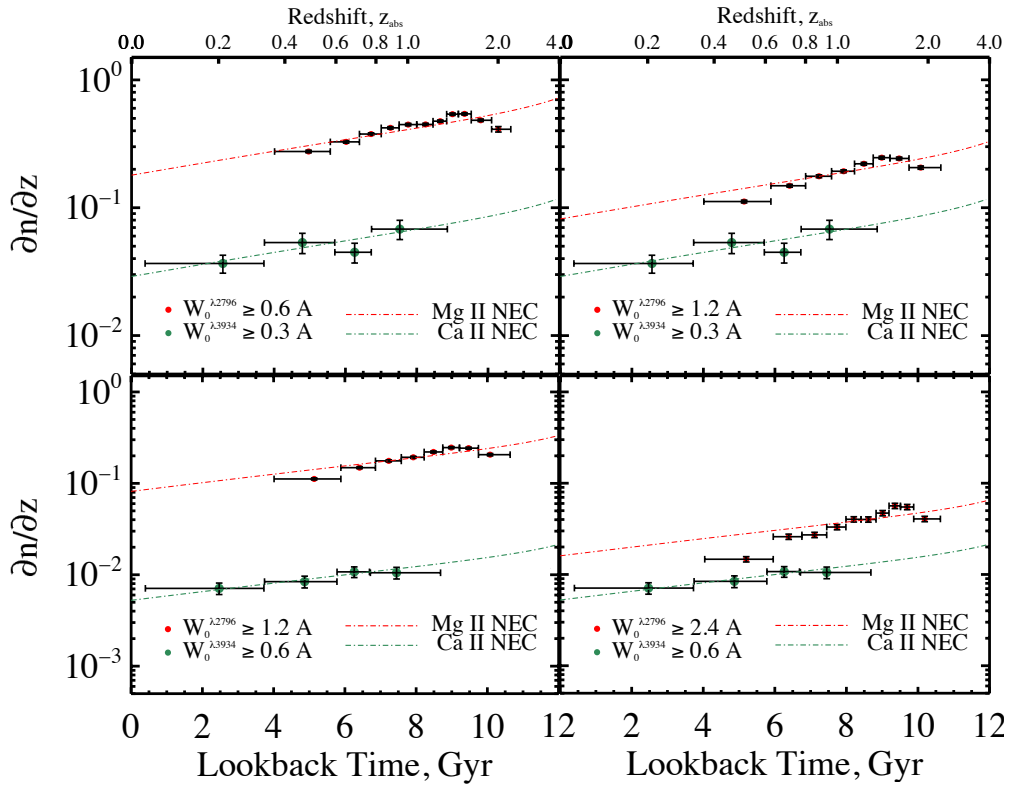


Figure 15. The Ca II incidence as a function of the z_{abs} across various $W_0^{\lambda 3934}$ thresholds. The no evolution curve is shown as dash dot lines. The errors are propagated using the Poisson errors.

All four single exponential functions fit the data in their corresponding subsamples at a better than 99% confidence level. Moreover, the MLE slopes for both subsamples with $W_0^{\lambda 3934} < 0.7 \text{ \AA}$ (left panels) are consistent with the W_{wk}^* value for the overall sample to within the errors, and the MLE slopes for both subsamples with $W_0^{\lambda 3934} > 0.7 \text{ \AA}$ (right panels) are consistent with the W_{str}^* value to within the errors. Also, dividing the entire sample at $DR=1.5$ into two subsamples yielded the same two component distribution specified in Equation 4 to within the errors.

Thus, at that accuracy of our data, the Ca II DR alone does not play a role in separating the Ca II absorbers into two populations. A series of KS tests were also performed and found to support this conclusion.

4.2 Trends with $W_0^{\lambda 3934}$ and $W_0^{\lambda 2796}/W_0^{\lambda 3934}$

For almost all Ca II absorbers with redshifts $z > 0.4$ we have information on the corresponding Mg II absorption. Therefore, we can explore if Mg II information can be used to isolate the two components of the $W_0^{\lambda 3934}$ distribution. From past work we know that Mg II absorption doublets found in SDSS surveys are generally saturated (Quider et al. 2011). As explained in §3.3, this means that Mg II rest equivalent widths are more representative of low-ionization gas velocity spreads rather than Mg^+ column densities. However, the Ca II doublet is generally unsaturated or only partially saturated, so to some degree the Ca II rest equivalent widths must be representative of Ca^+ column densities.

In Figure 17 we plot the two observed $W_0^{\lambda 2796}/W_0^{\lambda 3934}$ ratio histograms for Ca II absorbers with $W_0^{\lambda 3934} < 0.7 \text{ \AA}$ and $W_0^{\lambda 3934} \geq 0.7 \text{ \AA}$. This separation value is the same as the one used in §4.1 and is again motivated by our desire to roughly equalize the number of systems in each of two subsamples. There are ~ 120 absorbers in each subsample.

By using this $W_0^{\lambda 3934}$ separation value and including Mg II information, we produced Figure 17, which shows the Ca II absorbers to be a bimodal population, with the weaker Ca II absorbers having a larger (on average) and wider spread in $W_0^{\lambda 2796}/W_0^{\lambda 3934}$ than the stronger Ca II absorbers. A simple KS-test renders the two distributions inconsistent with one another at a $> 99\%$ confidence level. This bimodality provides supporting evidence that stronger and weaker Ca II absorbers (i.e., absorbers with relatively higher and lower Ca^+ column density values) may be different populations. We note that with the exception of a few data points, the Mg II absorbers associated with the Ca II absorbers have saturated doublets, which means that $W_0^{\lambda 2796}$ values are indicative of gas velocity spreads. See Figure 17 and its caption for color-coded data points (online version only) on Mg II doublet ratios and some additional explanation.

Finally, in Figure 18 we show that for those Ca II absorbers with Mg II information, it is possible to separate the $W_0^{\lambda 3934}$ distribution shown in Figure 7 into two single power-law distributions over the entire range of $W_0^{\lambda 3934}$ values. This is done by forming two subsamples divided at a $W_0^{\lambda 2796}/W_0^{\lambda 2803}$ ratio of ~ 1.8 , but in this case the subsamples are not approximately of equal size.

The slope of the steeper distribution is found to be consistent with the slopes of the weak component of the distribution in Figure 7 and the top-left and bottom-left panels

of Figure 16 (i.e with $W_0^{\lambda 3934} < 0.7 \text{ \AA}$). Similarly, the flatter red distribution is also consistent with the corresponding results for the strong systems in Figures 7 and 16.

5 SUMMARY AND CONCLUSIONS

We have presented the results of a blind survey for intervening Ca II absorption-line systems using $\sim 95,000$ quasar spectra from the seventh and ninth data release of the SDSS. Our results represent the largest compilation of Ca II absorbers to date. The rest wavelengths of the Ca II $\lambda\lambda 3934, 3969$ doublet resonance transition allow us to probe redshifts $z \lesssim 1.34$, which corresponds to the most recent ~ 8.9 Gyrs of the history of the Universe. Ca II absorbers are considerably more rare than Mg II absorbers. However, it is notable that with the original SDSS spectrograph, Mg II absorbers at $z \lesssim 0.4$ are not accessible. Therefore, studies of Ca II absorbers in quasar spectra are the only absorption-line systems which are generally accessible with SDSS spectra at $z \lesssim 0.4$, which is equivalent to the past ~ 4.3 Gyrs of cosmic time. Consequently, within the SDSS spectral window Ca II presents a unique opportunity for ground-based studies of cool, metal-rich gas around galaxies at the lowest redshifts, and such studies can help to constrain models for the existence of cool gas in the extended gaseous halos of galaxies.

Our blind survey resulted in the identification of 435 Ca II absorbers at rest equivalent width significance levels $\geq 5\sigma$ for $W_0^{\lambda 3934}$ and $\geq 2.5\sigma$ for $W_0^{\lambda 3969}$, within the physically-allowable doublet ratio range, i.e., $1 - \sigma_{DR} \leq W_0^{\lambda 3934}/W_0^{\lambda 3969} \leq 2 + \sigma_{DR}$. Of these detections, 251 Ca II absorbers at $z \gtrsim 0.4$ were found to have associated Mg II absorption, which is essentially all of them.

The sensitivity-corrected $W_0^{\lambda 3934}$ distribution cannot be fitted by a single-component exponential function, but a two-component exponential function describes the data well. We find $\partial n/\partial W_0^{\lambda 3934} = (N_{wk}^*/W_{wk}^*)exp(-W_0^{\lambda 3934}/W_{wk}^*) + (N_{str}^*/W_{str}^*)exp(-W_0^{\lambda 3934}/W_{str}^*)$, with $N_{wk}^* = 0.140 \pm 0.029$, $W_{wk}^* = 0.165 \pm 0.020 \text{ \AA}$, $N_{str}^* = 0.024 \pm 0.020$, and $W_{str}^* = 0.427 \pm 0.101 \text{ \AA}$. This suggests that the Ca II absorbers are composed of at least two distinct populations (Figure 7).

The Ca II absorber incidence was found to not evolve in the standard cosmology, implying that the product of integrated Ca II absorber cross section and their comoving number density has remained roughly constant over the last ~ 8.9 Gyrs. The normalization of the no-evolution curve, which is also the incidence extrapolated to $z = 0$, is $n_0 = 0.017 \pm 0.001$ for the sample with $W_0^{\lambda 3934} \geq 0.3 \text{ \AA}$.

Furthermore, we have demonstrated that the incidence of Ca II absorbers relative to the more common Mg II absorbers in quasar spectra is about 3 to 10 times smaller, depending on the REW threshold used for the comparison (Figure 15).

Finally, we performed some investigations to determine if we could use available Ca II absorber properties, specifically doublet ratio and Mg II information, to isolate the “weak” and “strong” populations of Ca II absorbers. While it was not possible to do this using the Ca II doublet ratio, we did find that Mg II information could be used to isolate the two populations (Figures 16 and 17).

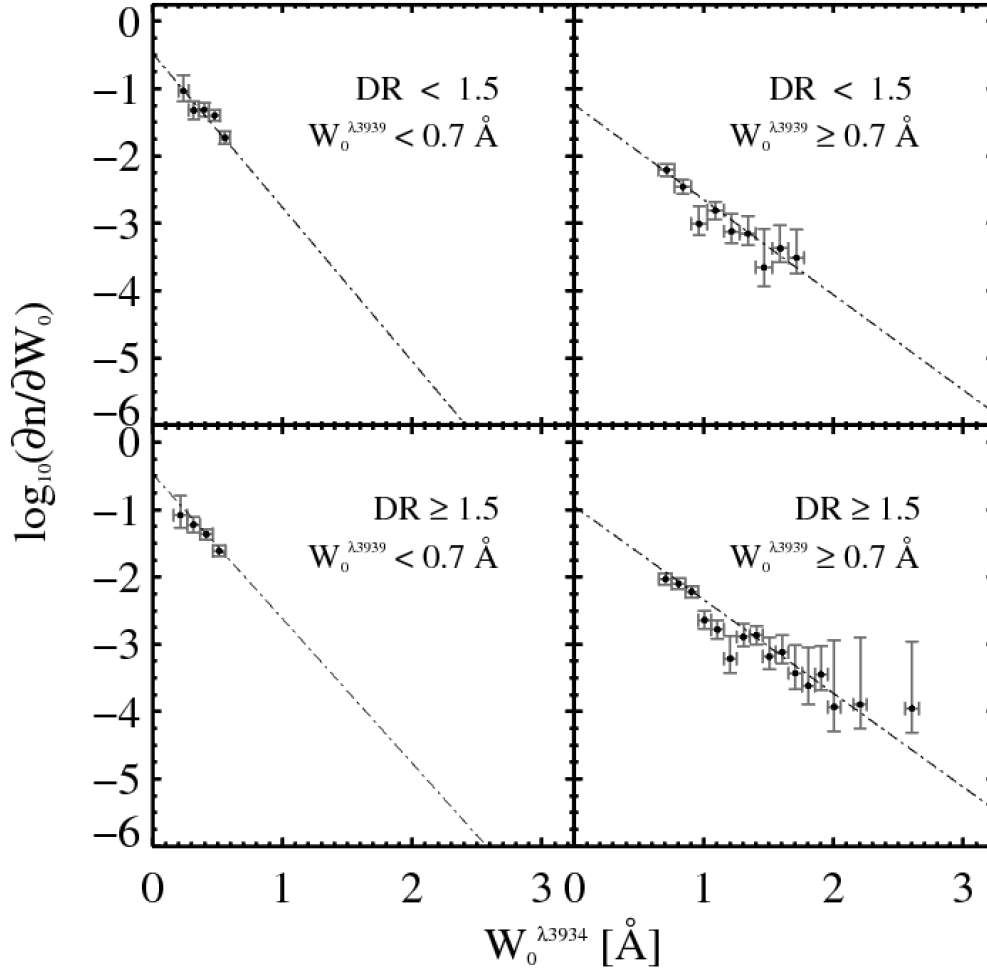


Figure 16. The sensitivity-corrected equivalent width distributions for four roughly equal subsamples of Ca II absorbers divided according to Ca II DR and $W_0^{\lambda 3934}$. The dash-dot lines are the MLE single power-law fits.

REFERENCES

- Ahn C. P. et al., 2012, *ApJS*, 203, 21
 Davé R., Finlator K., Oppenheimer B. D., 2011, *MNRAS*, 416, 1354
 Davé R., Oppenheimer B. D., Finlator K., 2011, *MNRAS*, 415, 11
 Dawson K. S. et al., 2013, *AJ*, 145, 10
 Dekel A., Birnboim Y., 2006, *MNRAS*, 368, 2
 Kereš D., Katz N., Fardal M., Davé R., Weinberg D. H., 2009, *MNRAS*, 395, 160
 Komatsu E. et al., 2011, *ApJS*, 192, 18
 Kramida A., Yu. Ralchenko, Reader J., and NIST ASD Team, 2013. NIST Atomic Spectra Database (ver. 5.1), [Online]. Available: <http://physics.nist.gov/asd> [2014, April 7]. National Institute of Standards and Technology, Gaithersburg, MD.
 Liddle A. R., 2007, *MNRAS*, 377, L74
 Murray N., Ménard B., Thompson T. A., 2011, *ApJ*, 735, 66
 Nath B. B., Silk J., 2009, *MNRAS*, 396, L90
 Nestor D. B., Pettini M., Hewett P. C., Rao S., Wild V., 2008, *MNRAS*, 390, 1670
 Nestor D. B., Turnshek D. A., Rao S. M., 2005, *ApJ*, 628, 637
 Noterdaeme P., Ledoux C., Petitjean P., Srianand R., 2008, *A&A*, 481, 327
 Noterdaeme P. et al., 2012, *A&A*, 547, L1
 Pâris I. et al., 2012, *A&A*, 548, A66
 Quider A. M., Nestor D. B., Turnshek D. A., Rao S. M., Monier E. M., Weyant A. N., Busche J. R., 2011, *AJ*, 141, 137
 Rao S. M., Turnshek D. A., Nestor D. B., 2006, *ApJ*, 636, 610
 Rimoldini L. G., 2007, PhD thesis, University of Pittsburgh
 Routly P. M., Spitzer, Jr. L., 1952, *ApJ*, 115, 227
 Savage B. D., Sembach K. R., 1996, *ARAA*, 34, 279
 Schlegel D. J. et al., 2007, in *Bulletin of the American Astronomical Society*, Vol. 39, American Astronomical Society Meeting Abstracts, p. 132.29
 Schneider D. P. et al., 2010, *AJ*, 139, 2360
 Seyffert E. N., Cooksey K. L., Simcoe R. A., O’Meara J. M., Kao M. M., Prochaska J. X., 2013, *ApJ*, 779, 161
 Sharma M., Nath B. B., 2012, *ApJ*, 750, 55
 Shen Y. et al., 2011, *ApJS*, 194, 45
 Smee S. A. et al., 2013, *AJ*, 146, 32
 Spergel D. N. et al., 2007, *ApJS*, 170, 377
 Stewart K. R., Kaufmann T., Bullock J. S., Barton E. J., Maller A. H., Diemand J., Wadsley J., 2011, *ApJ*, 735, L1
 Werk J. K. et al., 2014, *ArXiv e-prints*
 Wild V., Hewett P. C., 2005, *MNRAS*, 361, L30
 Wild V., Hewett P. C., Pettini M., 2006, *MNRAS*, 367, 211
 Wild V., Hewett P. C., Pettini M., 2007, *MNRAS*, 374, 292
 York D. G. et al., 2000, *AJ*, 120, 1579
 Zhu G., Ménard B., 2013, *ApJ*, 770, 130
 Zych B. J., Murphy M. T., Hewett P. C., Prochaska J. X., 2009,

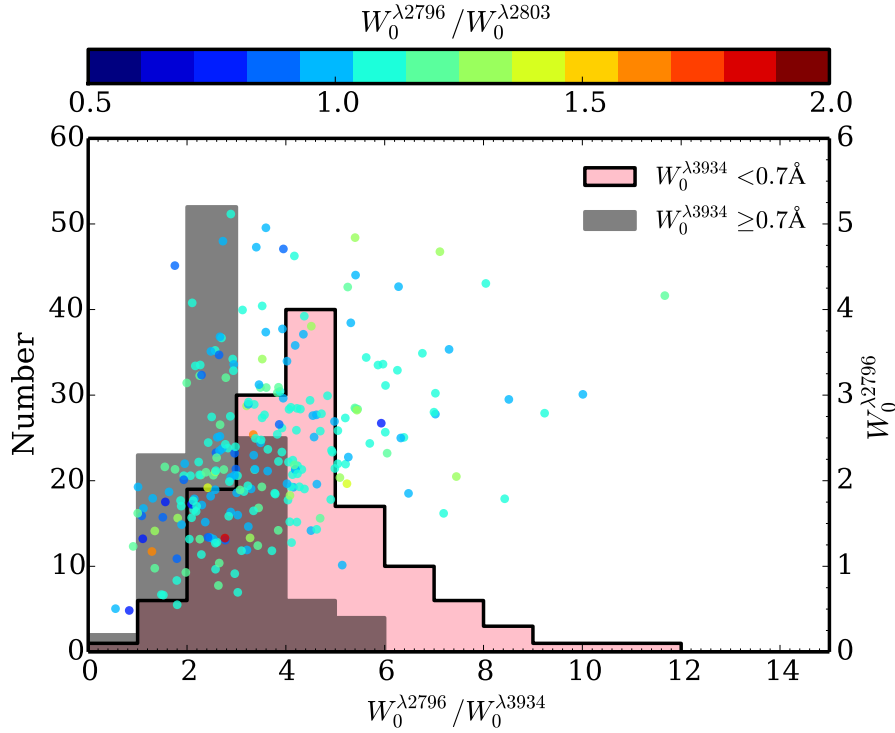


Figure 17. The bimodal distribution of the $W_0^{\lambda 2796}/W_0^{\lambda 2803}$ ratio for the weak and strong Ca II absorbers divided at $W_0^{\lambda 3934} = 0.7$ Å. Note that on this same figure we also plot $W_0^{\lambda 2796}/W_0^{\lambda 3934}$ (x-axis) as a function of $W_0^{\lambda 2796}$ (right y-axis); these data points are color-coded (online version only) according to the top color bar to show the saturation level of the Mg II doublet.

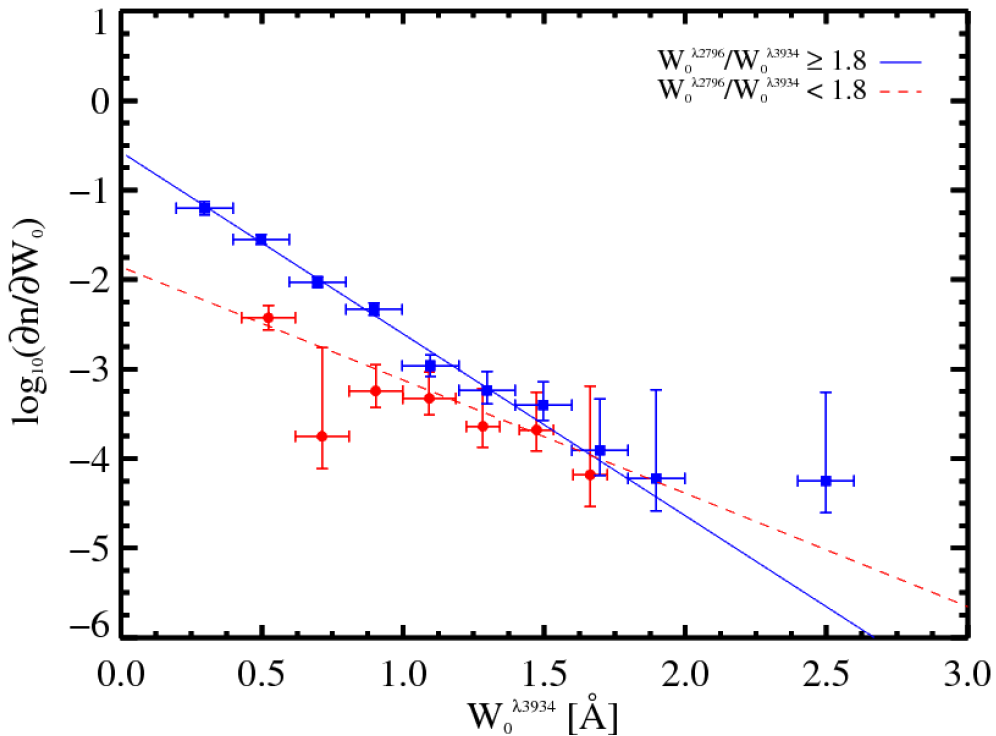


Figure 18. The sensitivity-corrected equivalent width distributions for two subsamples of Ca II absorbers separated at $W_0^{\lambda 2796}/W_0^{\lambda 3934} = 1.8$. The separation into two single power law fits is clear. The blue squares and red circles represent the subsamples with a $W_0^{\lambda 2796}/W_0^{\lambda 3934}$ ratio greater than and less than 1.8, respectively. The solid blue and dashed red lines are the best-fit single-exponential MLE fits to the unbinned distributions.

MNRAS, 392, 1429

Zych B. J., Murphy M. T., Pettini M., Hewett P. C., Ryan-Weber
E. V., Ellison S. L., 2007, MNRAS, 379, 1409

ACKNOWLEDGMENTS

GMS acknowledges support from a Zaccheus Daniel Fellowship and a Dietrich School of Arts and Sciences Graduate Fellowship and PITT PACC Fellowship from the University of Pittsburgh. We thank Eric Monier for providing his list of DR7 MgII absorbers to us (in order to supplement the DR4 list of Quider et al. (2011)) prior to publication. We thank Dan Nestor for making his continuum fitting software available for this work.

Funding for SDSS has been provided by the Alfred P. Sloan Foundation, the Participating Institutions, the National Science Foundation, and the US Department of Energy Office of Science. The SDSS is managed by the Astrophysical Research Consortium for the Participating Institutions. The Participating Institutions are the American Museum of Natural History, Astrophysical Institute Potsdam, University of Basel, University of Cambridge, Case Western Reserve University, University of Chicago, Drexel University, Fermilab, the Institute for Advanced Study, the Japan Participation Group, Johns Hopkins University, the Joint Institute for Nuclear Astrophysics, the Kavli Institute for Particle Astrophysics and Cosmology, the Korean Scientist Group, the Chinese Academy of Sciences (LAMOST), Los Alamos National Laboratory, the Max-Planck-Institute for Astronomy (MPIA), the Max-Planck-Institute for Astrophysics (MPA), New Mexico State University, Ohio State University, University of Pittsburgh, University of Portsmouth, Princeton University, the United States Naval Observatory, and the University of Washington.